



## Article

# Enhanced Thermochromic Performance of VO<sub>2</sub> Nanoparticles by Quenching Process

Senwei Wu , Longxiao Zhou, Bin Li, Shouqin Tian \* and Xiujian Zhao \*

State Key Laboratory of Silicate Materials for Architectures, Wuhan University of Technology (WUT), No. 122, Luoshi Road, Wuhan 430070, China; senwei\_wu@whut.edu.cn (S.W.); zhoulongxiao@whut.edu.cn (L.Z.); libin625@whut.edu.cn (B.L.)

\* Correspondence: tiansq@whut.edu.cn (S.T.); opluse@whut.edu.cn (X.Z.)

**Abstract:** Vanadium dioxide (VO<sub>2</sub>) has been a promising energy-saving material due to its reversible metal-insulator transition (MIT) performance. However, the application of VO<sub>2</sub> films has been seriously restricted due to the intrinsic low solar-energy modulation ability ( $\Delta T_{\text{sol}}$ ) and low luminous transmittance ( $T_{\text{lum}}$ ) of VO<sub>2</sub>. In order to solve the problems, the surface structure of VO<sub>2</sub> particles was regulated by the quenching process and the VO<sub>2</sub> dispersed films were fabricated by spin coating. Characterizations showed that the VO<sub>2</sub> particles quenched in deionized water or ethanol reserved VO<sub>2</sub>(M) phase structure and they were accompanied by surface lattice distortion compared to the pristine VO<sub>2</sub>. Such distortion structure contributed to less aggregation and highly individual dispersion of the quenched particles in nanocomposite films. The corresponding film of VO<sub>2</sub> quenched in water exhibited much higher  $\Delta T_{\text{sol}}$  with an increment of 42.5% from 8.8% of the original VO<sub>2</sub> film, because of the significant localized surface plasmon resonance (LSPR) effect. The film fabricated from the VO<sub>2</sub> quenched in ethanol presented enhanced thermochromic properties with 15.2% of  $\Delta T_{\text{sol}}$  and 62.5% of  $T_{\text{lum}}$ . It was found that the excellent  $T_{\text{lum}}$  resulted from the highly uniform dispersion state of the quenched VO<sub>2</sub> nanoparticles. In summary, the study provided a facile way to fabricate well-dispersed VO<sub>2</sub> nanocomposite films and to facilitate the industrialization development of VO<sub>2</sub> thermochromic films in the smart window field.

**Keywords:** VO<sub>2</sub>; quenching process; dispersion structure; thermochromic properties



**Citation:** Wu, S.; Zhou, L.; Li, B.; Tian, S.; Zhao, X. Enhanced

Thermochromic Performance of VO<sub>2</sub> Nanoparticles by Quenching Process. *Nanomaterials* **2023**, *13*, 2252. <https://doi.org/10.3390/nano13152252>

Academic Editor: Fabrizio Pirri

Received: 10 July 2023

Revised: 29 July 2023

Accepted: 3 August 2023

Published: 4 August 2023



**Copyright:** © 2023 by the authors. Licensee MDPI, Basel, Switzerland. This article is an open access article distributed under the terms and conditions of the Creative Commons Attribution (CC BY) license (<https://creativecommons.org/licenses/by/4.0/>).

## 1. Introduction

Since Morin F. J. discovered the reversible metal-insulator transition (MIT) behavior of vanadium oxides in 1959 [1], VO, V<sub>2</sub>O<sub>3</sub>, VO<sub>2</sub>, V<sub>6</sub>O<sub>13</sub>, V<sub>3</sub>O<sub>7</sub>, and V<sub>2</sub>O<sub>5</sub> [1–3] have been reported undergoing MIT at different ambient temperatures and showing significant gaps of the electrical, optical, magnetic properties before and after the MIT. Among them, the phase transition temperature ( $T_c$ ) of VO<sub>2</sub>, 341 K (68 °C), is the closest to room temperature, which makes VO<sub>2</sub> a promising candidate for intelligent film for smart windows. Below  $T_c$ , the strong electron-correlated VO<sub>2</sub> is monoclinic (M phase, P<sub>2</sub><sub>1</sub>/c) and highly transparent to NIR, which helps warm up the indoor room. When the ambient temperature rises above  $T_c$ , the VO<sub>2</sub> crystal transits to be tetragonal (R phase, P<sub>4</sub><sub>2</sub>/mnm) and reflective to the NIR, which is beneficial for blocking out the thermal radiation and cooling down the room temperature. Such characteristic of temperature-sensitive response of VO<sub>2</sub> is expected to enable intelligent regulation of indoor temperature, thereby reducing the energy consumption of architectures [2–4].

However, challenges remain in balancing the admirable luminous transmittance ( $T_{\text{lum}}$ ) for illuminance and the appreciable solar-energy modulation ability ( $\Delta T_{\text{sol}}$ ) for temperature regulations [5–7]. Such problems severely hinder the application of VO<sub>2</sub> thermochromic smart windows. Up till now, plenty of strategies have been dedicated to the performance optimization of VO<sub>2</sub>. Element doping is confirmed to be an effective way to diminish the

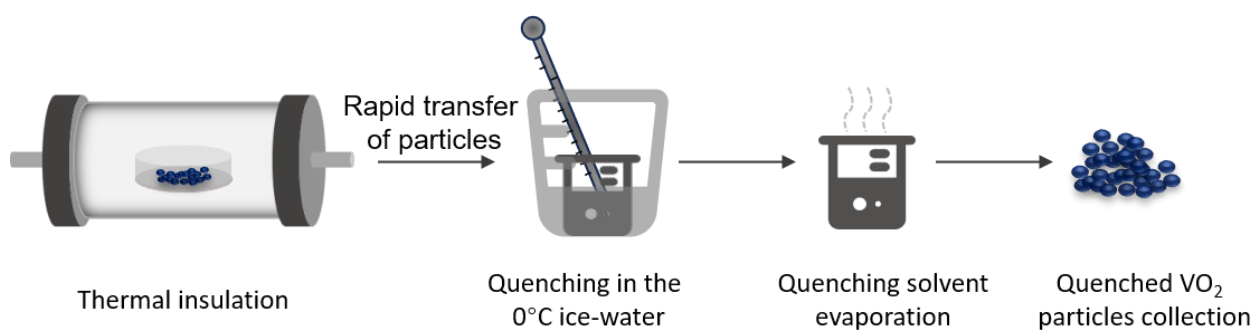
yellow color and boost the visible transmittance  $T_{lum}$  [3,5,8], and F [9], Mg [9,10], Ti [11], and Zr [12] are common dopants. Besides, VO<sub>2</sub> nano-/microstructure engineering [4], such as porous structure [13,14], grid structure [15], and biomimetic patterning [16] of VO<sub>2</sub> film, has been testified to cater for the optimization of thermochromic properties. In addition, multilayer construction [17–19] based on VO<sub>2</sub> film becomes an effective approach to enhance thermochromic properties, including but not limited to oxide buffer layers [20], antireflection layers [21], and noble metal layers [22]. Apart from multilayer structure, VO<sub>2</sub> nanocomposite coating by means of distributing VO<sub>2</sub> particles into matrix materials is another feasible way to improve  $T_{lum}$  and  $\Delta T_{sol}$ . When the ambient temperature is above  $T_c$ , the VO<sub>2</sub>(R) nanoparticles, with grain size much smaller than the wavelength of the incident light, present the localized surface plasma resonance (LSPR) effect around 1200 nm. Such an effect enables to enlarge the absorption and decreased transmittance of the infrared light. On the other hand, VO<sub>2</sub>(M) nanoparticles below  $T_c$  do not possess the characteristic of LSPR and the corresponding films are highly transparent to NIR. Such a NIR transmittance gap between VO<sub>2</sub>(M) and VO<sub>2</sub>(R) results in much higher  $\Delta T_{sol}$ . Additionally, the transparent matrix covering isolated particles gives rise to higher  $T_{lum}$  of the VO<sub>2</sub> nanocomposite coatings. Typically, SiO<sub>2</sub> [23], SnO<sub>2</sub> [24], TiO<sub>2</sub> [25], and Si-Al oxide [26] are common inorganic matrixes for VO<sub>2</sub> nanoparticles. Unfortunately, these matrixes require a strict annealing atmosphere or precisely uniform dispersion of VO<sub>2</sub> in the nanocomposite films. Compared to inorganic matrix, organic agents, such as polyvinyl pyrrolidone (PVP) [13,27], polyurethane (PU) [28], polyvinyl butyral (PVB) [29], and acrylic resin [30], have become more favorable hosts due to their low refractive index and facile fabrication process. Gao et al. [31] synthesized a flexible coating by dispersing SiO<sub>2</sub> capsuled monocrystal VO<sub>2</sub> with good crystallinity, fine grain size (VO<sub>2</sub>@SiO<sub>2</sub>) into PU, which showed good optical properties ( $T_{lum} = 55.3\%$ ,  $\Delta T_{sol} = 7.5\%$ ). In addition, they further developed a roll-coated VO<sub>2</sub> nanocomposite coating with smoothness, uniformity, and high transparency on 1200 × 1000 mm<sup>2</sup> large-scale glass. By modulating the viscosity of the host PU, Zou et al. [32] upgraded the solar modulation ability of VO<sub>2</sub>/PU composite film from 6.6% to 14.5%, whereas the luminous transmittance was maintained 54%. On the other hand, PVP was widely reported to be an alternative matrix. Zhao et al. [13] mixed VO<sub>2</sub> nanoparticles, ZnO nanoparticles, and PVP to fabricate a composite film, successfully enhancing  $T_{lum}$  from 54.9% to 63.9% and improving  $\Delta T_{sol}$  from 9.9% to 11.3%. Recently, Tian et al. [33] demonstrated an in-situ synthesis route to coat VO<sub>2</sub> nanocomposite on the glass surface by PVP decomposition and a mass transfer process during annealing, achieving remarkable optical performance with  $T_{lum}$  of 72.5% and  $\Delta T_{sol}$  of 10.1%. Yet, there were rare reports about the interactions between the VO<sub>2</sub> and the matrix.

In this work, high-purity VO<sub>2</sub>(M) particles obtained by a one-step annealing process were quenched to induce surface structural distortion. Deionized water and ethanol were used as the quenching solvents to modulate the surface structure of VO<sub>2</sub> particles. As it turned out, the phase transition temperature of the quenched powders was slightly reduced by around 3 °C. In addition, the quenched VO<sub>2</sub> nanoparticles were dispersed individually in the PVP when spin-coated to form the VO<sub>2</sub> nanocomposite films. Such dispersion structures contributed to the optimization of the thermochromic properties of the film. It was discovered that the quenched VO<sub>2</sub> particles showed high dispersity in the nanocomposite films and presented an evident LSPR effect, which contributed to the enhanced solar-energy modulation ability of the films. Moreover, the film fabricated by the ethanol-quenched VO<sub>2</sub> uncovered excellent optical performance, accompanied by  $\Delta T_{sol}$  of 15.2% and  $T_{lum}$  of 62.5%. The outstanding performance successfully achieved the simultaneous enhancement of both solar energy modulation ability and luminous transmittance of the film, and it was superior to most of the VO<sub>2</sub> nanocomposite films in previous reports [21,23,27,31–33] that failed to make a positive balance of  $\Delta T_{sol}$  and  $T_{lum}$ . Herein, this work provided a facile quenching process to benefit the thermochromic performance of VO<sub>2</sub> composite film and to drive its application in smart windows.

## 2. Methods

### 2.1. Fabrication of Quenched VO<sub>2</sub>(M) Nanoparticles

All reagents that were used directly were analytically pure and provided by Sinopharm Chemical Reagent Co., Ltd, Shanghai, China. A certain mass of vanadium pentoxide (V<sub>2</sub>O<sub>5</sub>, 0.8 g) powders and half the amount of ammonium bicarbonate (NH<sub>4</sub>HCO<sub>3</sub>, 0.4 g) particles were loaded together in a quartz crucible and then transferred into the tube furnace. The furnace was pumped below 50 Pa and heated around 550 °C until the powders changed to dark-blue VO<sub>2</sub> particles. After that, the particles were processed with quenching treatment as Scheme 1 described. In detail, VO<sub>2</sub> particles were placed in a vacuum tube furnace for thermal insulation treatment for half an hour and then they were rapidly moved into the 0 °C quenching solution surrounded by an ice-water system. Extra ice bulks were constantly added to the system so that the quenching solvent was maintained at around 0 °C. Next, the beaker holding the above-mentioned solution mixed with quenched VO<sub>2</sub> grains was put in a thermostatic oven to completely evaporate the solvent. Finally, the remaining nanoparticles in the beaker were collected as quenched VO<sub>2</sub>(M).



**Scheme 1.** Diagram of the quenching process of the VO<sub>2</sub> particles.

### 2.2. Fabrication of VO<sub>2</sub>-PVP Nanocomposite Film

The obtained VO<sub>2</sub>(M) nanoparticles were mixed with polyvinylpyrrolidone (PVP, K30) and ethanol in the mill tank. Intermittent ball milling gave rise to particles with smaller sizes to achieve thorough dispersion in the ethanol. Afterward, the mixture liquid was transferred into a centrifuge tube for solid-liquid separation. The upper liquid in the tube remained turbid as VO<sub>2</sub> with extreme fine sizes dispersed well in PVP, which dissolved well in ethanol. With the evaporation of liquid in the upper suspension, VO<sub>2</sub>-PVP nanocomposites were collected and then made into a coating slurry by mixing them with additional ethanol. Continuous stirring and ultrasonic vibration were implemented to make the slurry homogeneous. Then spin-coating was carried out to form a sol/wet film by dropping the solution on a common soda-lime-silica glass substrate. In the end, ethanol was removed by heating to form the VO<sub>2</sub>-PVP nanocomposite films.

### 2.3. Characterization

X-ray diffraction (XRD, D8DISCOVER, Bruker, Billerica, MA, USA) with Cu K $\alpha$  ( $\lambda = 0.154056$  nm) serving as the source of radiation, and 3 kW of the output power) was adopted to determine the phase structures of the powders over the  $2\theta$  between 10° and 80°. A differential scanning calorimeter (DSC, DSC8500, PerkinElmer, Waltham, MA, USA) was used to examine the phase transition temperature of the powders with the temperature ranging from 0 °C to 100 °C at the rate of 5 °C/min in the heating/cooling loop, as illustrated in Equation (1).  $T_c$  refers to the average phase transition temperature of VO<sub>2</sub> particles.  $T_{c,h}$  and  $T_{c,c}$  correspond to the phase transition temperature peak of VO<sub>2</sub> in the heating and cooling stages, respectively. A field emission scanning electron microscopy (FE-SEM, Zeiss Ultra Plus, Carl Zeiss CMP GmbH, Oberkochen, Germany) was used to observe the morphology of both the composite powders and films. X-ray photoelectron spectroscopy (XPS, ESCALAB 250Xi, ThermoFisher, Waltham, MA, USA) was utilized to determine the

element composition and valence. FT–IR spectrum (Nicolet6700, ThermoFisher, Waltham, MA, USA) was served to identify the functional groups of the samples.

$$T_c = (T_{c,h} + T_{c,c})/2 \quad (1)$$

The thermochromic performance of the films was measured from 300 to 2500 nm by a UV–vis–NIR spectrophotometer (UV-3600) equipped with a temperature-controlling device. The transmittance of the films at 20 °C and 90 °C corresponded to VO<sub>2</sub>(M) and VO<sub>2</sub>(R), respectively. The integrated luminous transmittance ( $T_{lum}$ , 380 nm ≤ λ ≤ 780 nm) and solar transmittance ( $T_{sol}$ , 300 nm ≤ λ ≤ 2500 nm) can be calculated according to Equations (2) and (3).

$$T_{lum} = \frac{\int \varphi_{lum}(\lambda)T(\lambda)d\lambda}{\int \varphi_{lum}(\lambda)d\lambda} \quad (2)$$

$$T_{sol} = \frac{\int \varphi_{sol}(\lambda)T(\lambda)d\lambda}{\int \varphi_{sol}(\lambda)d\lambda} \quad (3)$$

In the equations,  $T(\lambda)$  represents the film transmittance of light at a certain wavelength (λ),  $\varphi_{lum}(\lambda)$  is the standard luminous efficiency function for the photopic vision of human eyes [11], and  $\varphi_{sol}(\lambda)$  is the solar irradiance spectrum for air mass 1.5 corresponding to the sun standing 37° above the horizon.  $\Delta T_{sol}$  is the difference value of  $T_{sol}$  at 20 °C and 90 °C, as given in Equation (4).

$$\Delta T_{sol} = T_{sol}(20\text{ °C}) - T_{sol}(90\text{ °C}) \quad (4)$$

### 3. Results and Discussion

#### 3.1. Structure of the VO<sub>2</sub> Nanoparticles

VO<sub>2</sub> powders were obtained from V<sub>2</sub>O<sub>5</sub> by a facial annealing reduction reaction. As shown in the TG-DSC pattern (Figure 1a) of the mixture of V<sub>2</sub>O<sub>5</sub> and NH<sub>4</sub>HCO<sub>3</sub>, NH<sub>4</sub>HCO<sub>3</sub> kept decomposing to release NH<sub>3</sub> at the beginning during the homogeneous heating period, illustrating the continuous mass loss of the raw materials. Till 183.5 °C, NH<sub>4</sub>HCO<sub>3</sub> decomposed completely and the mass loss in this period was 8.28% in total. The endothermic peak at 226.2 °C indicated that the absorbed H<sub>2</sub>O was released, accounting for 3.29% of the reaction agents. With the rising temperature, the reducibility of NH<sub>3</sub> contributed to changing the vanadium (V) in V<sub>2</sub>O<sub>5</sub> to lower valence, accompanied by an exothermic process at 360.0 °C, and finally reached the stable phase until 400 °C, as no mass loss or well as energy exchange could be observed in the pattern. This result suggested that 400 °C was suitable for V<sub>2</sub>O<sub>5</sub> reduction. Additionally, the small temperature deviation between DSC and DTG could be attributed to the errors caused by the test instrument. Figure 1b showed the XRD patterns of the VO<sub>2</sub> samples annealed from V<sub>2</sub>O<sub>5</sub> and NH<sub>4</sub>HCO<sub>3</sub> mixture at 400 °C, 450 °C, 550 °C, and 550 °C. Although the main diffraction peaks (27.8°, 35.7°, 37.8°, and 55.8°) matched well with VO<sub>2</sub>(M) (PDF #44-0252), extra peaks with evident intensity (25.3°, 33.5°, and 49.5°) belonging to V<sub>6</sub>O<sub>13</sub> (PDF #27-1318) could be observed for the samples obtained at 400 °C, which meant the incomplete reduction of V<sub>2</sub>O<sub>5</sub> to V<sub>6</sub>O<sub>13</sub>. Such a result disagreed with the ideal reaction temperature in Figure 1a. The reason could be attributed to the fact that the furnace chamber in the annealing process was too large, and the effective heating interval of the furnace was small, which caused partial energy loss. When raising the annealing temperature to 450 °C, the fabricated samples came across the same situation. Interestingly, the diffraction peaks belonging to V<sub>6</sub>O<sub>13</sub> of the VO<sub>2</sub> sample reduced at 450 °C were much weaker than those of VO<sub>2</sub> reduced at 400 °C, testifying that the proportion of V<sub>6</sub>O<sub>13</sub> among the VO<sub>2</sub> samples annealed at 450 °C was much less than that of the VO<sub>2</sub> annealed at 400 °C. Thus, a higher annealing temperature was demanded to overcome the energy barrier for reducing V<sub>2</sub>O<sub>5</sub> into VO<sub>2</sub> thoroughly. In addition, it turned out that the material annealed at 500 °C became pure VO<sub>2</sub>(M) with sharp diffraction peaks. Such peaks implied that the 500 °C reduced VO<sub>2</sub>

featured excellent crystallinity. Comparably, the powders annealed at 550 °C remained pure VO<sub>2</sub>(M) structure but exhibited a decreased peak intensity, indicating worse crystallinity of the related VO<sub>2</sub> powders. This might be caused by the unexpected grain agglomeration during the thermal insulation at higher temperatures. Therefore, 500 °C was selected as the ideal temperature to produce pristine VO<sub>2</sub> (labeled as P-VO<sub>2</sub>).

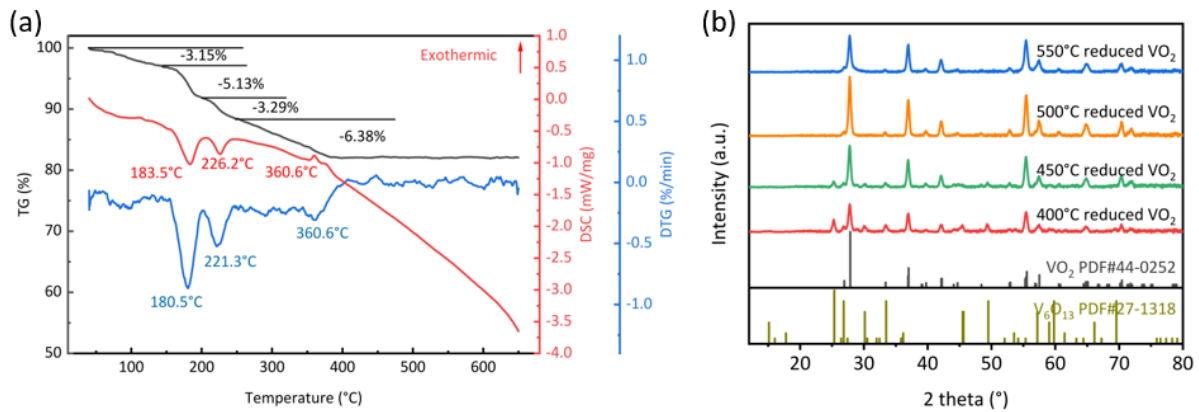


**Figure 1.** (a) TG-DSC pattern of the V<sub>2</sub>O<sub>5</sub> and NH<sub>4</sub>HCO<sub>3</sub> raw mixture and (b) XRD pattern of VO<sub>2</sub> powders annealed at different temperatures.

To observe the metal-insulator transition, P-VO<sub>2</sub> was characterized through in-situ XRD technique, and the results were shown in Figure 2a,b, and Figure 2b was the enlarged view of the pink area in Figure 2a. The VO<sub>2</sub> stayed the monoclinic structure below 45 °C, and the main peak (27.76°) corresponded to the (011) crystal plane of VO<sub>2</sub>(M). When the temperature rose above 65 °C, the peak shifted to 27.63°, revealing that the VO<sub>2</sub> crystals had transferred to the rutile phase, featured with the (110) crystal plane of VO<sub>2</sub>(R) (PDF #73-2362). This phenomenon suggested that the phase transition temperature of P-VO<sub>2</sub> ranged between 45 °C and 65 °C. This was in agreement with previous reports [5] for VO<sub>2</sub> particles. When the VO<sub>2</sub> particles cooled down from 75 °C to 65 °C, VO<sub>2</sub> crystals transited back to monoclinic structure from rutile structure. This helped observe the evident and reversible MIT behavior between VO<sub>2</sub>(M) and VO<sub>2</sub>(R) in the previous report [34]. Furthermore, the phase transition temperature of the cooling stage was inconsistent with that of the heating stage, confirming the thermal hysteresis loop feature of VO<sub>2</sub> in the phase transition stage. It was the MIT behavior that made VO<sub>2</sub> a promising material for smart windows.

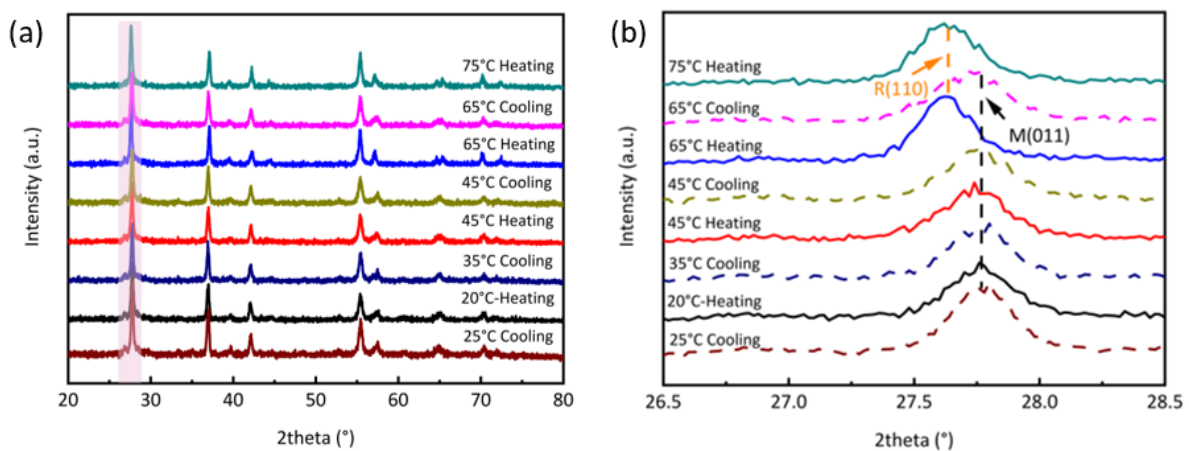


**Figure 2.** (a) In-situ XRD pattern of P-VO<sub>2</sub> and (b) enlarged view of the diffraction angle ranging from 26.5° to 28.5° in the heating and cooling stages.

In order to cause surface distortion for the crystal, P-VO<sub>2</sub> featured with the notable MIT behavior was placed in a 0 °C ice-water system for quenching treatment as Scheme 1 il-

illustrated. According to the difference in quenching solvent, the VO<sub>2</sub> quenched in deionized water was named H-VO<sub>2</sub> and the one quenched in ethanol was noted as E-VO<sub>2</sub>. The XRD pattern of VO<sub>2</sub> under different quenching solvents was shown in Figure 3a. Compared to the pristine VO<sub>2</sub> without the quenching process, both the H-VO<sub>2</sub> and E-VO<sub>2</sub> powders held the phase structure of VO<sub>2</sub>(M) in Figure 1b. A smaller peak located at 25.3° appeared in the quenched samples, which could be the localized oxidation caused by exposure to air during powder transfer. It is worth noting that quenched particles presented the VO<sub>2</sub>(M) phase and manifested great crystallinity. In addition, surface lattice distortion of the VO<sub>2</sub> was assumed to occur after the quenching process [35], which would be discussed in the next part. According to the Scherrer equation, the average grain size of E-VO<sub>2</sub> and H-VO<sub>2</sub> were calculated as 30.08 nm and 17.06 nm, respectively, larger than the average size (12.11 nm) of P-VO<sub>2</sub>. To explain the mean grain size changes of the three samples, an enlarged view of the XRD diffraction angle ranging from 27.0° to 28.5° (Organe area in Figure 3a) was presented to illustrate the half-width changes of the peaks. As shown in Figure 3b, the diffraction curve of P-VO<sub>2</sub> exhibited the greatest widening state compared to E-VO<sub>2</sub> and H-VO<sub>2</sub>. Such a state endowed P-VO<sub>2</sub> with the largest half-width and thus, the smallest grain size among the three particles. On the other hand, the half-width of the E-VO<sub>2</sub> (011) crystal plane diffraction peak was approaching that of H-VO<sub>2</sub>. However, the diffraction peak of E-VO<sub>2</sub> shifted to a higher position at 27.91°, compared to the peak at 27.86° of P-VO<sub>2</sub>. Such a shift to a higher angle caused the fact that the grain size of E-VO<sub>2</sub> was a bit larger than that of H-VO<sub>2</sub>. This phenomenon might be attributed to the hydroxy group attached to the surface of VO<sub>2</sub> when the heated particles encountered an ice-water/ice-ethanol system and thus, leading to surface lattice distortion of the crystals. Moreover, thermal insulation during the quenching process in Scheme 1 was also beneficial to grain growth.

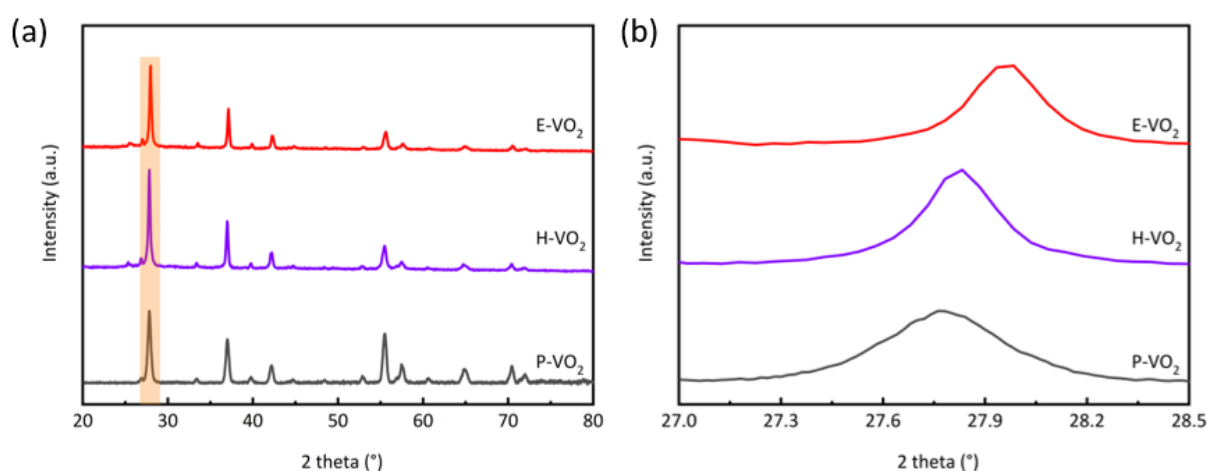


**Figure 3.** (a) XRD pattern of P-VO<sub>2</sub>, H-VO<sub>2</sub>, and E-VO<sub>2</sub> powders and (b) enlarged view of the diffraction angle ranging from 27.0° to 28.5°.

With the goal of further determining the effect of the quenching process on VO<sub>2</sub>, the XPS technique was used to identify the chemical environment of elements, and the results were presented in Figure 4. Regarding the C1s peak at 284.80 eV as the calibration position, the full spectrum (Figure 4a) illustrated the existence of vanadium and oxygen in all the P-VO<sub>2</sub>, H-VO<sub>2</sub>, and E-VO<sub>2</sub> powders according to the V2p and O1s peaks. The V2p peaks were analyzed by Advantage of Thermo Scientific. In addition, Shirley background subtraction was employed to diminish the influence of heightened peaks due to signals from electrons undergoing inelastic scattering during the XPS characterization, ensuring a convincing quantification analysis of the peaks. As the high-resolution pattern for V2p shown in Figure 4b to d, both the V2p<sub>3/2</sub> and V2p<sub>1/2</sub> spectral peaks were significantly asymmetrical and each was split into two peaks, which implied that the vanadium of all the VO<sub>2</sub> samples involved two different chemical states, corresponding to V<sup>4+</sup> (The fitted

purple curve) and  $V^{5+}$  (The fitted green curve), respectively.  $V^{5+}$  owing to  $V_2O_5$  consisted of  $V2p_{3/2}$  at 517.5 eV and  $V2p_{1/2}$  at 525.0 eV. The gap between the  $V2p_{3/2}$  orbital and  $V2p_{3/2}$  orbital was 7.5 eV, which is in line with previous work [13]. Additionally, it is supposed that the existence of  $V^{5+}$  was caused by partial oxidation when the  $VO_2$  particles were exposed to air [36]. The  $V^{4+}$  attributed to  $VO_2$  was made up of  $V2p_{3/2}$  at 516.2 eV and  $V2p_{1/2}$  at 523.7 eV. In addition, the  $V2p_{3/2}$  of P- $VO_2$  was most occupied with  $V^{5+}$ , and  $V^{4+}$  only accounted for a small proportion. Comparably, the  $V^{4+}$  in the  $V2p$  orbitals of H- $VO_2$  in Figure 4c showed the highest percentage, followed by E- $VO_2$  in Figure 4d, and finally, the P- $VO_2$  declared the least  $V^{4+}$  content in Figure 4b. Such results could be attributed to the surface lattice distortion of H- $VO_2$  and E- $VO_2$ .

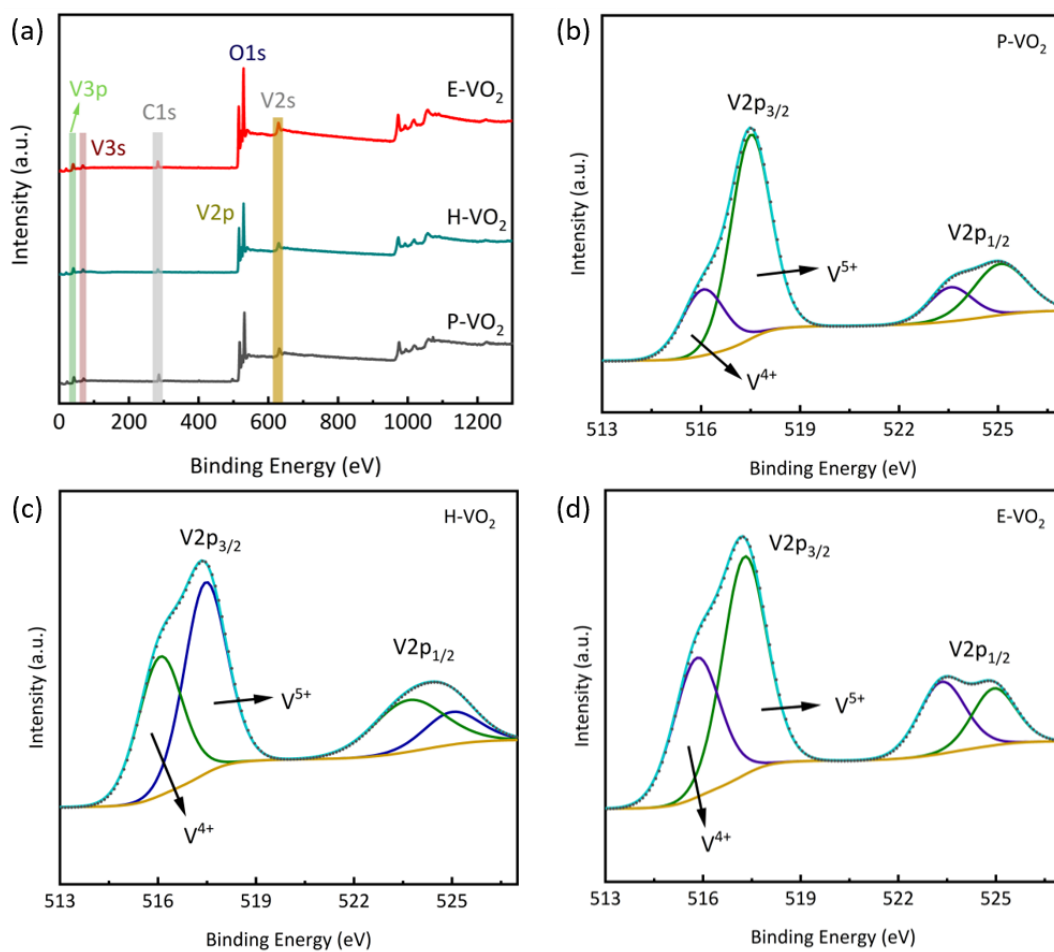


**Figure 4.** (a) XPS spectrum comparison of  $VO_2$  powders and the high-resolution patterns for  $V2p$  of P- $VO_2$  (b), H- $VO_2$  (c), and E- $VO_2$  (d).

SEM was employed to investigate the morphology of the aforementioned  $VO_2$  particles. Due to the large size of the commercial precursor  $V_2O_5$ , the directly annealed P- $VO_2$  particles inherited the large grain size, as shown in Figure 5a. It is evident that the particles aggregated severely to form large-scale clusters, with irregular shapes and different sizes ranging from 0.2  $\mu\text{m}$  to 1.2  $\mu\text{m}$ . Unfortunately, such sizes hindered P- $VO_2$  from dispersing in the PVP matrix for film coating. Compared to the pristine sample, the degree of particle aggregation of quenched  $VO_2$  was much improved. In Figure 5b, the big clusters were broken into small H- $VO_2$  parts with varying sizes, showing that the deionized water was able to split the large-size P- $VO_2$  gathering during the quenching process. Especially, when the quenched solvent was replaced with ethanol with a smaller density, E- $VO_2$  interacted more severely with the liquid and turned more entire separation into nanoparticles with approximately 200 nm in size, as presented in Figure 5c. In addition, the voids clearly

appeared among the E-VO<sub>2</sub> nanoparticles and the linkage knot hinted the E-VO<sub>2</sub> separated from large-size P-VO<sub>2</sub> particles. The observation that the quenched VO<sub>2</sub> nanoparticles were easily separated into small pellets from large-sized clusters resulted from the thermodynamically unstable state of these aggregated clusters. This unstable state was due to the surface crystal distortion caused by the quenching process, confirming the results of XPS spectrums. It is worth mentioning that the particle was much larger than the value calculated in Figure 3a. The fact that the XRD resulted from Cu K $\alpha$  radiation reflected crystalline particles rather than the actual morphology of the powders might explain the difference in the mean particle sizes. As for SEM, the signals of secondary electrons with much smaller De Broglie wavelengths were collected to reflect the topography of the particles. The different wavelengths of Cu K $\alpha$  in XRD and secondary electrons in SEM caused different imaging results. On the other hand, VO<sub>2</sub> particles in Figure 5 were assumed to be polycrystalline consisting of substantial crystals.

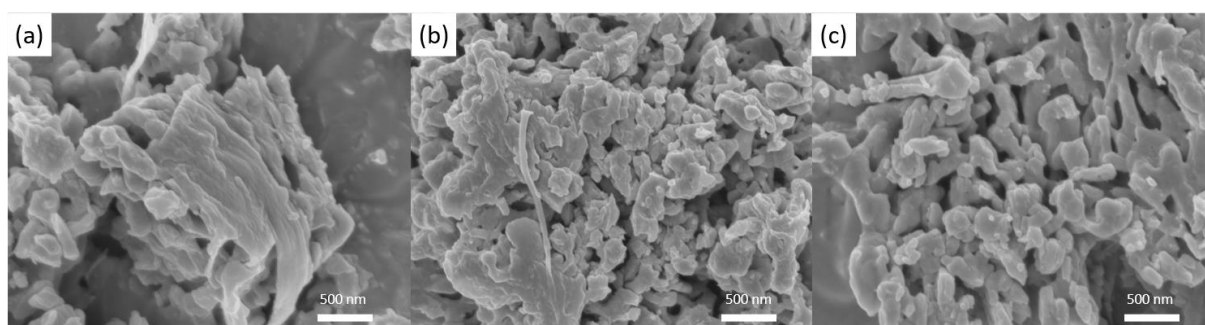


**Figure 5.** SEM images of (a) P-VO<sub>2</sub>, (b) H-VO<sub>2</sub>, and (c) E-VO<sub>2</sub> powders.

The DSC curves of the above P-VO<sub>2</sub> H-VO<sub>2</sub> and E-VO<sub>2</sub> powders are illustrated in Figure 6a with expected exothermic and endothermic peaks. Such a thermal energy change suggested the phase transition behavior between VO<sub>2</sub>(M) and VO<sub>2</sub>(R). The exothermic peak ( $T_{c,h}$ ) at 68.35 °C and endothermic peak ( $T_{c,c}$ ) at 61.09 °C of P-VO<sub>2</sub> implied the average  $T_c$  was 64.72 °C according to Equation (1). On the other hand, the energy involved in the MIT behavior was 47 J/g, approaching 51 J/g of the bulk VO<sub>2</sub>, showing good crystallinity of P-VO<sub>2</sub> powders as shown in Figure 2. With the quenching process, the H-VO<sub>2</sub> powders with phase transition peaks at 65.61 °C and 58.53 °C presented the average  $T_c$  as 62.07 °C, while the  $T_c$  of E-VO<sub>2</sub> nanoparticles was calculated as 62.73 °C from the  $T_{c,h}$  peak at 65.73 °C and  $T_{c,c}$  peak at 58.24 °C. It is clear that the  $T_c$  of the quenched samples was slightly lowered, which could be attributed to the surface lattice distortion of the VO<sub>2</sub> crystal structure as the XPS results suggested.

Considering the similar structure of H<sub>2</sub>O and C<sub>2</sub>H<sub>6</sub>O, FT-IR was employed to detect the -OH bond of the VO<sub>2</sub> particles. In Figure 6b, the -OH bond corresponded to the peaks at 3450 cm<sup>-1</sup> and hydrogen bonds appeared at 1630 cm<sup>-1</sup>. The integral area of the peak at 1630 cm<sup>-1</sup> was used to reflect the relative content of the hydroxyl group in the samples. It turned out that the hydroxyl peak area of H-VO<sub>2</sub> particles was the largest at 106.4, followed by the peak area of 87.7 of E-VO<sub>2</sub>, and finally the value of 25.3 of P-VO<sub>2</sub>. Such results indicated that the absorbed hydroxyl on the surface of both H-VO<sub>2</sub> and E-VO<sub>2</sub> particles was more than P-VO<sub>2</sub>. This could be due to the surface lattice distortion of the quenched samples, so there were more absorption sites bound to the hydroxyl group on the surface of these particles. Additionally, the peaks at around 990 cm<sup>-1</sup> and 890 cm<sup>-1</sup>, respectively, corresponded to the stretching vibration and asymmetric stretching vibration of the V=O bond. The overlapping peaks at 720 cm<sup>-1</sup> and 660 cm<sup>-1</sup> were the characteristic peaks of VO<sub>2</sub>(M) [37]. In addition, the peaks at around 530 cm<sup>-1</sup> were labeled as the stretching vibration of the V-O-V bond. Apart from the peak offset of the corresponding bonds in VO<sub>2</sub>, small extra peaks at around 1285 m<sup>-1</sup> were discovered in H-VO<sub>2</sub> and E-VO<sub>2</sub>, which was

attributed to the O-H band after the quenching process. Such a phenomenon confirmed the surface lattice distortion to VO<sub>2</sub> crystals of H-VO<sub>2</sub> and E-VO<sub>2</sub>.

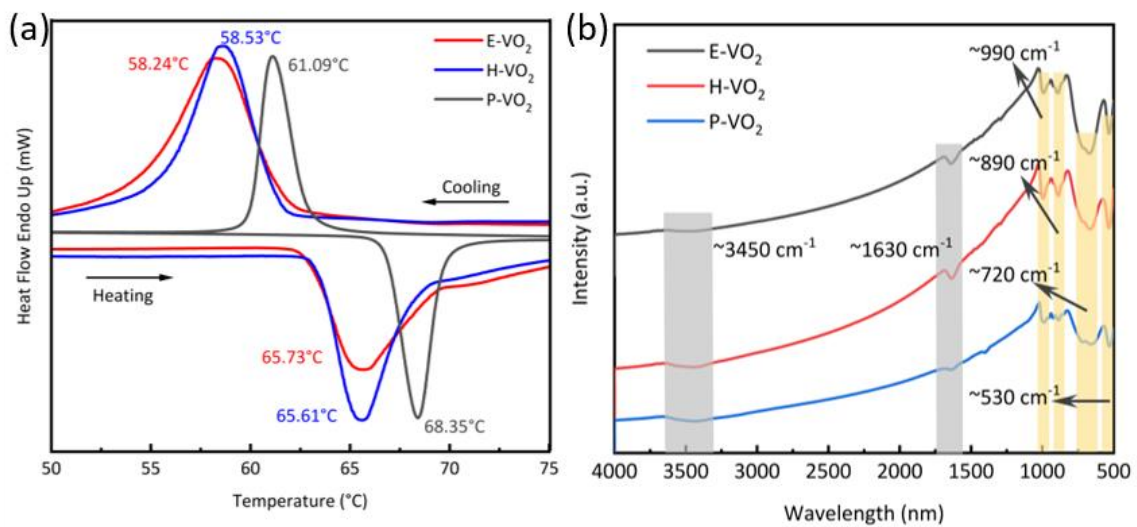


**Figure 6.** (a) DSC curve and (b) FT-IR spectrum of P-VO<sub>2</sub>, H-VO<sub>2</sub>, and E-VO<sub>2</sub> powders.

### 3.2. Thermochromic Properties and Morphology of VO<sub>2</sub> Nanocomposite Films

To reduce the grain size of the as-synthesized particles, VO<sub>2</sub> samples were mixed with PVP and ethanol in the mill tank to conduct thorough ball milling and centrifugation, ending up with a dark liquid mixture. The turbid upper solution was dried to collect the VO<sub>2</sub>-PVP compound, which was then mixed with additional ethanol to configure the spin-coating slurry. The slurry was then dropped on the soda-lime-silica glass substrate and spun to form the VO<sub>2</sub> nanocomposite films. A UV3600 spectrophotometer coupled with a temperature-controlling device was served to characterize the transmittance of the films ranging from 300 nm to 2500 nm, and the thermochromic properties of the VO<sub>2</sub> nanocomposite films were integrated by Equations (2) to (4). The solid lines in Figure 7a were tested at 20 °C, revealing the transmittance of M phase VO<sub>2</sub> samples, and the dash lines were obtained at 90 °C, appearing the transmittance of R phase VO<sub>2</sub> samples. As shown in Figure 7a and Table 1, the  $T_{lum}$  of P-VO<sub>2</sub> film was 53.2% and  $\Delta T_{sol}$  just reached 8.8%. The grain accumulation in Figure 5a was the cause for such poor properties. Comparably, the H-VO<sub>2</sub> film sacrificed a small amount of luminous transmittance of 3.1% to achieve as enormous as 42.5% of improvement in solar-energy modulation ability to reach 12.5%. The reason for the enhanced  $\Delta T_{sol}$  originated from the LSPR absorption peak of H-VO<sub>2</sub> located at 1258 nm, which was stronger than the P-VO<sub>2</sub> peak at 1293 nm. Such a phenomenon led to an enlarged gap in the transmittance of VO<sub>2</sub> at 20 °C and 90 °C and contributed to higher  $\Delta T_{sol}$ . The E-VO<sub>2</sub> nanocomposite film that came across with the same LSPR effect at 1150 nm revealed an exceeding increment of  $\Delta T_{sol}$  of 72.2% (from 8.8% to 15.2%). In addition, the  $T_{lum}$  of E-VO<sub>2</sub> film was boosted to 62.5%, indicating a better dispersity of the VO<sub>2</sub> nanoparticles in the PVP matrix. The optimized luminous transmittance was also credited for less aggregation of the nanoparticles as shown in Figure 5c. In Figure 7b, the thermochromic performance of E-VO<sub>2</sub> in this work was compared to previously reported VO<sub>2</sub> nanocomposite films, and it was clear that the E-VO<sub>2</sub> film exceeded most VO<sub>2</sub> films [21,23,27,31–33]. Besides, the excellent  $\Delta T_{sol}$  of the E-VO<sub>2</sub> film was able to satisfy the demands of effectively regulating room temperature while the great  $T_{lum}$  met the requirement of indoor brightness, which was a great achievement for the potential application of VO<sub>2</sub> thermochromic smart windows.

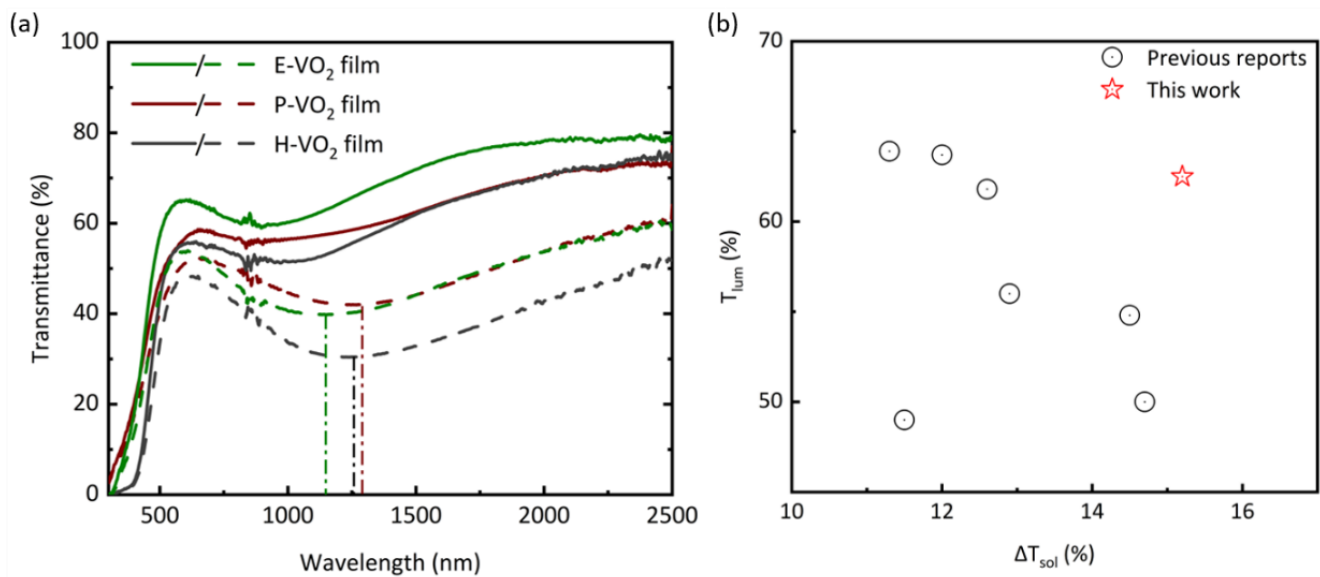


**Figure 7.** (a) Transmittance spectrum comparison of VO<sub>2</sub> films and (b) thermochromic performance comparison between this work and previously reported VO<sub>2</sub> nanocomposite films.

**Table 1.** Thermochromic properties of different VO<sub>2</sub> films.

Sample	$T_{sol}$ (%)		$T_{lum}$ (%)		$\Delta T_{sol}$ (%)	$\Delta T_{NIR}$ (%)
	20 °C	90 °C	20 °C	90 °C		
P-VO <sub>2</sub> film	52.5	43.7	53.2	47.3	8.8	12.8
H-VO <sub>2</sub> film	47.9	35.4	51.6	43.5	12.5	19.8
E-VO <sub>2</sub> film	58.2	43.0	62.5	50.9	15.2	21.1

The morphology of the films was presented. It is clear that P-VO<sub>2</sub> turned into nanoparticles with a size of around 100 nm after a ball milling process as described in Figure 8a. However, particle aggregation in Figure 5a was still common even though they were spin-coated to film. This aggregation structure was the reason for the unsatisfied thermochromic properties of the P-VO<sub>2</sub> film. Comparably, grain accumulation also existed in H-VO<sub>2</sub> film, which caused low luminous transmittance of the film. Additionally, cracks could be found in the film, and they were the cause of the inadequate performance of  $T_{lum}$ . It is worth mentioning that most H-VO<sub>2</sub> nanoparticles exhibited much smaller sizes than P-VO<sub>2</sub> and they were dispersed individually in the PVP in Figure 8b, causing the LSPR effect and the improvement of  $\Delta T_{sol}$ . In Figure 8c, the E-VO<sub>2</sub> nanoparticles showed an average size of tens of nanometers and nearly no sign of particle aggregation. Additionally, these particles with surface lattice distortion were highly isolated from each other and uniformly dispersed in the E-VO<sub>2</sub> nanocomposite film. The large-scale surface morphology of E-VO<sub>2</sub> film in Figure 8d introduced such dispersity of VO<sub>2</sub> nanoparticles in a more intuitive perspective. This dispersion structure became beneficial for the optical properties of E-VO<sub>2</sub> nanocomposite film.

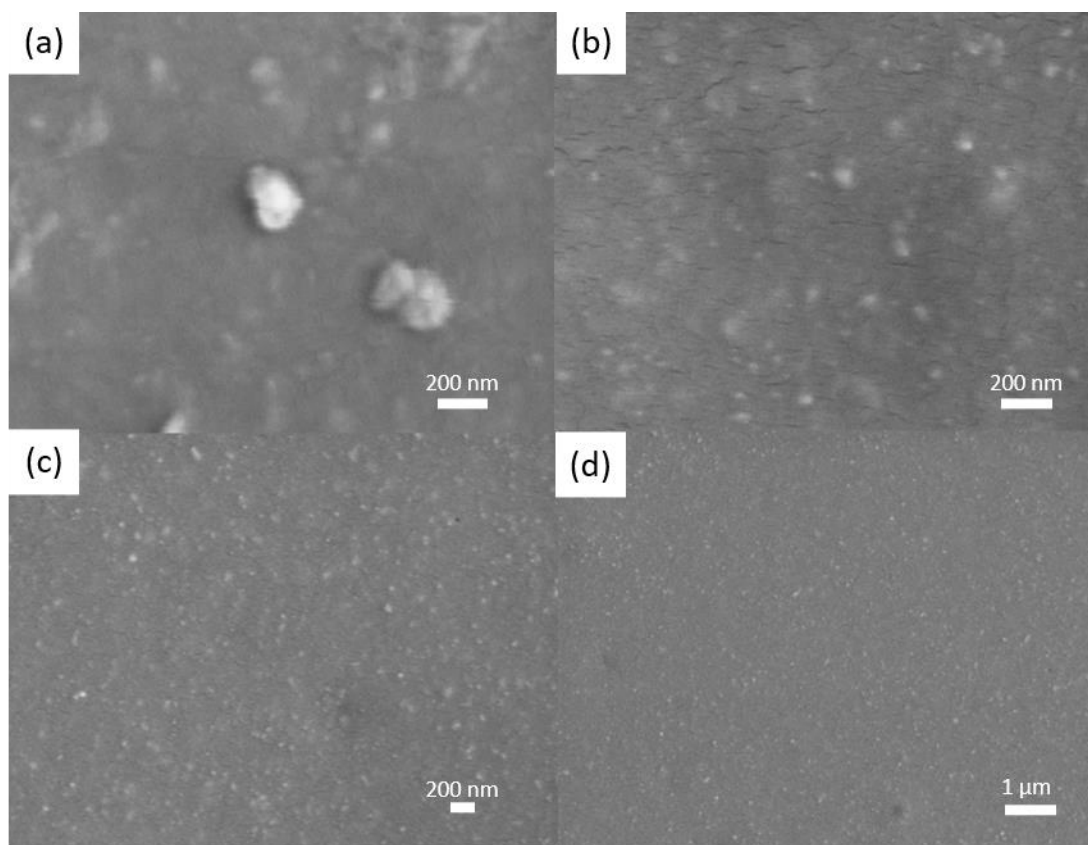


**Figure 8.** SEM images of (a) P-VO<sub>2</sub>, (b) H-VO<sub>2</sub>, and (c,d) E-VO<sub>2</sub> nanocomposite films.

#### 4. Conclusions

As a strong electronic associated material, VO<sub>2</sub>(M) underwent a reversible phase transition between the monoclinic phase and rutile phase, corresponding with an abrupt change of near-infrared light transmittance, thus showing great potential in the smart window application. To improve the thermochromic properties of VO<sub>2</sub>, this paper applied a facile annealing method to synthesize VO<sub>2</sub>(M) powders. With the quenching treatment, the VO<sub>2</sub> particles presented surface lattice distortion and they were individually dispersed in the PVP host to induce the LSPR effect, contributing to the exciting increment of solar-energy modulation ability. Hereby, the film corresponding to H-VO<sub>2</sub> achieved an enormous improvement in  $\Delta T_{\text{sol}}$  from 8.8% to 12.5%. Moreover, the film fabricated by the ethanol-quenched VO<sub>2</sub> with no sign of aggregation showed an exceedingly high  $\Delta T_{\text{sol}}$  of 15.2%, and the high dispersity of E-VO<sub>2</sub> nanoparticles in the film contributed to much enhanced  $T_{\text{lum}}$  of 62.5%. Therefore, this work provided a new thought to promote the thermochromic performance of VO<sub>2</sub> by particle quenching and the strategy was beneficial to the commercialization of VO<sub>2</sub> thermochromic smart windows.

**Author Contributions:** S.W. contributed to writing the original draft and conducting the experiment and data analysis. L.Z. contributed to characterizing the structure of the samples and B.L. was responsible for the optical performance characterization of the films. S.T. contributed to analyzing all the data and supervising the experimental routine and data analysis. X.Z. was involved in analyzing all the data and revising the manuscript. All authors have read and agreed to the published version of the manuscript.

**Funding:** This work was supported by the National Natural Science Foundation of China (Grant No. 51772229), the 111 project (No. B18038), the National Key R&D Program of China (No. 2017YFE0192600), Key R&D Project of Hubei Province (No. 2020BAB061), National innovation and entrepreneurship training program for college students (No. 201910497034), Open Foundation of the State Key Laboratory of Silicate Materials for Architectures at WUT (No. SYSJJ2021-05 and SYSJJ2022-01), State Key

Laboratory of Materials Processing and Die & Mould Technology, Huazhong University of Science and Technology (No. P2021-010).

**Institutional Review Board Statement:** Not applicable.

**Informed Consent Statement:** Not applicable.

**Data Availability Statement:** Data are available on request from the authors.

**Acknowledgments:** We also thank the Analytical and Testing Center of WUT for the help with carrying out the materials characterization.

**Conflicts of Interest:** The authors declare no potential conflict of financial interest with respect to the research.

## References

1. Morin, F.J. Oxides which show a metal-to-insulator transition at the neel temperature. *Phys. Rev. Lett.* **1959**, *3*, 34–36. [[CrossRef](#)]
2. Hu, P.; Hu, P.; Vu, T.D.; Li, M.; Wang, S.; Ke, Y.; Zeng, X.; Mai, L.; Long, Y. Vanadium oxide: Phase diagrams, structures, synthesis, and applications. *Chem. Rev.* **2023**, *123*, 4353–4415. [[CrossRef](#)]
3. Zhang, Z.; Zhang, L.; Zhou, Y.; Cui, Y.; Chen, Z.; Liu, Y.; Li, J.; Long, Y.; Gao, Y. Thermochromic energy efficient windows: Fundamentals, recent advances, and perspectives. *Chem. Rev.* **2023**, *123*, 7025–7080. [[CrossRef](#)]
4. Bhupathi, S.; Wang, S.; Ke, Y.; Long, Y. Recent progress in vanadium dioxide: The multi-stimuli responsive material and its applications. *Mater. Sci. Eng. R Rep.* **2023**, *155*, 100747. [[CrossRef](#)]
5. Gao, Y.; Luo, H.; Zhang, Z.; Kang, L.; Chen, Z.; Du, J.; Kanehira, M.; Cao, C. Nanoceramic VO<sub>2</sub> thermochromic smart glass: A review on progress in solution processing. *Nano Energy* **2012**, *1*, 221–246. [[CrossRef](#)]
6. Xu, F.; Cao, X.; Luo, H.; Jin, P. Recent advances in VO<sub>2</sub>-based thermochromic composites for smart windows. *J. Mater. Chem. C* **2018**, *6*, 1903–1919. [[CrossRef](#)]
7. Song, J.; Zhao, Y.; Sun, L.; Luo, Q.; Xu, H.; Wang, C.; Xin, H.; Wu, W.; Ma, F. VO<sub>2</sub>/ATO nanocomposite thin films with enhanced solar modulation and high luminous transmittance for smart windows. *Ceram. Int.* **2022**, *48*, 15868–15876. [[CrossRef](#)]
8. Ding, X.; Li, Y.; Zhang, Y. Sol-gel derived tungsten doped VO<sub>2</sub> thin films on Si substrate with tunable phase transition properties. *Molecules* **2023**, *28*, 3778. [[CrossRef](#)]
9. Abdellaoui, I.; Merad, G.; Maaza, M.; Abdelkader, H.S. Electronic and optical properties of Mg-, F-doped and Mg\F-codoped M1-VO<sub>2</sub> via hybrid density functional calculations. *J. Alloys Compd.* **2016**, *658*, 569–575. [[CrossRef](#)]
10. Panagopoulou, M.; Gagaoudakis, E.; Boukos, N.; Aperathitis, E.; Kiriakidis, G.; Tsoukalas, D.; Raptis, Y.S. Thermochromic performance of Mg-doped VO<sub>2</sub> thin films on functional substrates for glazing applications. *Sol. Energy Mater. Sol. Cells* **2016**, *157*, 1004–1010. [[CrossRef](#)]
11. Zhao, J.; Chen, D.; Hao, C.; Mi, W.; Zhou, L. The optimization and role of Ti surface doping in thermochromic VO<sub>2</sub> film. *Opt. Mater.* **2022**, *133*, 112960. [[CrossRef](#)]
12. Qin, S.; Fan, Y.; Qiu, X.; Gou, G.; Zhang, K.; Feng, Q.; Gan, G.; Sun, W. Modulation of the phase transition behavior of VO<sub>2</sub> nanofilms by the coupling of Zr doping and thickness-dependent band gap. *ACS Appl. Mater. Interfaces* **2022**, *4*, 6067–6075. [[CrossRef](#)]
13. Wu, S.; Tian, S.; Liu, B.; Tao, H.; Zhao, X.; Palgrave, R.G.; Sankar, G.; Parkin, I.P. Facile synthesis of mesoporous VO<sub>2</sub> nanocrystals by a cotton-template method and their enhanced thermochromic properties. *Sol. Energy Mater. Sol. Cells* **2018**, *176*, 427–434. [[CrossRef](#)]
14. Long, S.; Cao, X.; Wang, Y.; Chang, T.; Li, N.; Jin, L.; Ma, L.; Xu, F.; Sun, G.; Jin, P. Karst landform-like VO<sub>2</sub> single layer solution: Controllable morphology and excellent optical performance for smart glazing applications. *Sol. Energy Mater. Sol. Cells* **2020**, *209*, 110449. [[CrossRef](#)]
15. Ke, Y.; Wen, X.; Zhao, D.; Che, R.; Xiong, Q.; Long, Y. Controllable fabrication of two-dimensional patterned VO<sub>2</sub> nanoparticle, nanodome, and nanonet arrays with tunable temperature-dependent localized surface plasmon resonance. *ACS Nano* **2017**, *11*, 7542–7551. [[CrossRef](#)] [[PubMed](#)]
16. Qian, X.; Wang, N.; Li, Y.; Zhang, J.; Xu, Z.; Long, Y. Bioinspired multifunctional vanadium dioxide: Improved thermochromism and hydrophobicity. *Langmuir* **2014**, *30*, 10766–10771. [[CrossRef](#)]
17. Yao, L.; Qu, Z.; Sun, R.; Pang, Z.; Wang, Y.; Jin, B.; He, J. Long-lived multilayer coatings for smart windows: Integration of energy-saving, antifogging, and self-healing functions. *ACS Appl. Energy Mater.* **2019**, *2*, 7467–7473. [[CrossRef](#)]
18. Mlyuka, N.R.; Niklasson, G.A.; Granqvist, C.G. Thermochromic multilayer films of VO<sub>2</sub> and TiO<sub>2</sub> with enhanced transmittance. *Sol. Energy Mater. Sol. Cells* **2009**, *93*, 1685–1687. [[CrossRef](#)]
19. Long, S.; Zhou, H.; Bao, S.; Xin, Y.; Cao, X.; Jin, P. Thermochromic multilayer films of WO<sub>3</sub>/VO<sub>2</sub>/WO<sub>3</sub> sandwich structure with enhanced luminous transmittance and durability. *RSC Adv.* **2016**, *6*, 106435–106442. [[CrossRef](#)]
20. Panagopoulou, M.; Gagaoudakis, E.; Aperathitis, E.; Michail, I.; Kiriakidis, G.; Tsoukalas, D.; Raptis, Y.S. The effect of buffer layer on the thermochromic properties of undoped radio frequency sputtered VO<sub>2</sub> thin films. *Thin Solid Films* **2015**, *594*, 310–315. [[CrossRef](#)]

21. Yao, L.; Qu, Z.; Pang, Z.; Li, J.; Tang, S.; He, J.; Feng, L. Three-layered hollow nanospheres based coatings with ultrahigh-performance of energy-saving, antireflection, and self-cleaning for smart windows. *Small* **2018**, *14*, e1801661. [[CrossRef](#)] [[PubMed](#)]
22. Granqvist, C.G. Transparent conductors as solar energy materials: A panoramic review. *Sol. Energy Mater. Sol. Cells* **2007**, *91*, 1529–1598. [[CrossRef](#)]
23. Kang, J.; Liu, J.; Shi, F.; Dong, Y.; Song, X.; Wang, Z.; Tian, Z.; Xu, J.; Ma, J.; Zhao, X. Facile fabrication of VO<sub>2</sub>/SiO<sub>2</sub> aerogel nanocomposite films with excellent thermochromic properties for smart windows. *Appl. Surf. Sci.* **2022**, *573*, 151507. [[CrossRef](#)]
24. Li, D.; Deng, S.; Zhao, Z.; Yang, J.; Wang, B.; Li, J.; Jin, H. VO<sub>2</sub>(M)@SnO<sub>2</sub> core-shell nanoparticles: Improved chemical stability and thermochromic property rendered by SnO<sub>2</sub> shell. *Appl. Surf. Sci.* **2022**, *598*, 153741. [[CrossRef](#)]
25. Samal, A.; Lakshya, A.K.; Dhar Dwivedi, S.M.M.; Dalal, A.; Ghosh, A.; Paul, A.D.; Mahapatra, R.; Gupta, R.K.; Hasan, M.A.; Dey, A.; et al. Stable and reversible phase change performance of TiO<sub>2</sub> coated VO<sub>2</sub> nano-columns: Experiments and theoretical analysis. *Ceram. Int.* **2021**, *47*, 14741–14749. [[CrossRef](#)]
26. Liu, C.; Cao, X.; Kamyshny, A.; Law, J.Y.; Magdassi, S.; Long, Y. VO<sub>2</sub>/Si-Al gel nanocomposite thermochromic smart foils: Largely enhanced luminous transmittance and solar modulation. *J. Colloid Interface Sci.* **2014**, *427*, 49–53. [[CrossRef](#)]
27. Li, B.; Liu, J.; Tian, S.; Liu, B.; Yang, X.; Yu, Z.; Zhao, X. VO<sub>2</sub>-ZnO nanocomposite films with enhanced thermochromic properties for smart windows. *Ceram. Int.* **2020**, *46*, 2758–2763. [[CrossRef](#)]
28. Kang, J.; Liu, J.; Shi, F.; Dong, Y.; Jiang, S. The thermochromic characteristics of Zn-doped VO<sub>2</sub> that were prepared by the hydrothermal and post-annealing process and their polyurethane nanocomposite films. *Ceram. Int.* **2021**, *47*, 15631–15638. [[CrossRef](#)]
29. Cool, N.I.; Larriuz, C.A.; James, R.; Ayala, J.R.; Anita; Al-Hashimi, M.; Banerjee, S. Thermochromic fenestration elements based on the dispersion of functionalized VO<sub>2</sub> nanocrystals within a polyvinyl butyral laminate. *ACS Eng. Au* **2022**, *2*, 477–485. [[CrossRef](#)]
30. Mao, Z.; Huang, W.; Zhou, W.; Tang, L.; Shi, Q. In-situ stirring assisted hydrothermal synthesis of W-doped VO<sub>2</sub>(M) nanorods with improved doping efficiency and mid-infrared switching property. *J. Alloys Compd.* **2020**, *821*, 153556. [[CrossRef](#)]
31. Cao, C.; Yanfeng, G.; Hongjie, L. Pure single-crystal rutile vanadium dioxide powders: Synthesis, mechanism and phase-transformation property. *J. Phys. Chem. C* **2008**, *112*, 18810–18814. [[CrossRef](#)]
32. Yang, X.; Zou, J. Facile fabrication of VO<sub>2</sub> composite film with enhanced significantly solar modulation performance by adjusting viscosity of VO<sub>2</sub>/PU dispersion. *J. Alloys Compd.* **2023**, *940*, 168868. [[CrossRef](#)]
33. Li, B.; Tian, S.; Qian, J.; Wu, S.; Liu, B.; Zhao, X. In situ synthesis of highly dispersed VO<sub>2</sub>(M) nanoparticles on glass surface for energy efficient smart windows. *Ceram. Int.* **2023**, *49*, 2310–2318. [[CrossRef](#)]
34. Yuan, L.; Hu, Z.; Hou, C.; Meng, X. In-Situ thermochromic mechanism of Spin-Coated VO<sub>2</sub> film. *Appl. Surf. Sci.* **2021**, *564*, 150441. [[CrossRef](#)]
35. Liu, B.; Cheng, K.; Nie, S.; Zhao, X.; Yu, H.; Yu, J.; Fujishima, A.; Nakata, K. Ice-water quenching induced Ti<sup>3+</sup> self-doped TiO<sub>2</sub> with surface lattice distortion and the increased photocatalytic activity. *J. Phys. Chem. C* **2017**, *121*, 19836–19848. [[CrossRef](#)]
36. Li, B.; Tian, S.; Tao, H.; Zhao, X. Tungsten doped M-phase VO<sub>2</sub> mesoporous nanocrystals with enhanced comprehensive thermochromic properties for smart windows. *Ceram. Int.* **2019**, *45*, 4342–4350. [[CrossRef](#)]
37. Mohamed Azharudeen, A.; Karthiga, R.; Rajarajan, M.; Suganthi, A. Enhancement of electrochemical sensor for the determination of glucose based on mesoporous VO<sub>2</sub>/PVA nanocomposites. *Surf. Interfaces* **2019**, *16*, 164–173. [[CrossRef](#)]

**Disclaimer/Publisher's Note:** The statements, opinions and data contained in all publications are solely those of the individual author(s) and contributor(s) and not of MDPI and/or the editor(s). MDPI and/or the editor(s) disclaim responsibility for any injury to people or property resulting from any ideas, methods, instructions or products referred to in the content.